Chapter 8

Magnetic Resonance (MR)-transverse relaxivity in tri-magnetic ensemble of isotropic-anisotropic nanosystems having dynamic magnetic behaviour

8.1 INTRODUCTION

The morphology of primary MNPs in the ensemble can impact the MR-relaxivity [1-10], as the shape of MNPs shows a modification in magnetization and such modulation triggers enhanced MR-transverse relaxivity [10-19]. Moreover, basic MR-relaxivity theories can not explain the dephasing mechanism of water proton extensity if a complex structure is considered [20-30]. The consideration of classical and quantum methods, as explained in the previous chapters, is observed to be inconclusive [31, 33, 34] for complexity-induced ensembles of MNPs. However, shape anisotropy can monitor MR-relaxivity efficacy as anisotropic systems bear enhanced effective radius [30-33]. However, surface modifications in MNPs having either magnetic or non-magnetic systems, more dependent inherent parameters can be addressed for evaluating MR-relaxivity [29-33].

In a complex domain of ensembles, the dominance of long-range ordering can lower the magnetization, further reducing relaxivity [31]. The induced complexity can be modified intentionally if a hybrid system is considered, which can be considered a comprised framework of isotropic as well as anisotropic MNPs. This novel approach can trigger enhancement in the shape anisotropy. As a consequence, it can be considered as a promising way to attain enhancement of faster relaxation in MR-transverse relaxivity. Therefore, the dynamic nature of complex hybrid ensembles is required to draw a novel correlation among

inherent magnetic properties in highly anisotropic hybrid domains of interacting MNPs with MR-relaxivity regulations, for prevailing the residing mechanism for complex ensembles.

Herein this chapter, interacting SPM state dominance hybrid ensemble is considered where shape anisotropy is manipulated by introducing flower-shaped ensemble of 2D nanoflakes over spherical nanoparticles, γ-Fe$_2$O$_3$@δ-MnO$_2$@NiFe$_2$O$_4$. The correlation of MR-relaxivity efficiency with the aid of structural parameter modulation is addressed in this chapter. SAXS and SANS studies are performed for structural correlation investigation in the complex ensemble. However, the dynamic nature of interacting spins is studied and regulation in energy barrier having slow dynamics of spin shows significant transverse relaxivity. The enhanced shape anisotropy correlation in a framework of hierarchical ensemble is addressed to achieve potential merits in MR-relaxivity enhancement.

8.2 EXPERIMENTAL DETAILS

The synthesis is governed by four various steps [26, 27]. The chemicals used for synthesis are brought from Zenith India. The formation technique of the MnO$_2$@NiFe$_2$O$_4$ ensemble is similar to the synthesis technique explained in Chapter 3 [26]. Moreover, the development of maghemite is similar to the technique explained in Chapter 7 [27]. For hybrid system development, a needed amount of maghemite is dispersed in the solvent of chloroform and the already prepared MnO$_2$@NiFe$_2$O$_4$ ensembles are dispersed in maghemite dispersed homogeneous solution. With constant stirring followed by sonication for nearly 30 mins, a homogeneously dispersed final solution is achieved and kept for solvent evaporation under a vacuum at 60°C. Once the evaporation is completed, the powder is collected and taken for washing with the aid of deionized water. After overnight drying, the final sample is collected for further analysis. However, the used instrumental details are similar to previous chapters.

8.3 RESULTS AND DISCUSSIONS

8.3.1 Microstructural study

Field Emission Transition Electron Microscopy (FESEM) images are represented in Figure 8.1 which gives the details about the morphology of the ensembles. Isotropic MNP distribution is depicted over the nanoflakes of MnO_2 and some nano-assembles of maghemite are also shown in yellow in Figure 8.1 (b) for differentiation. The isotropic maghemite is observed over a few of the flakes, and few MNPs are residing between the MnO_2 flakes. The respective entrapment of MNPs inside the ensemble is triggered by a solvent evaporation method. The development of a complex ensemble is followed by Ostwald ripening for ensemble growth and oriented attachment for the growth of 2D flakes [26]. The schematic representation is shown in Figure 8.1 (f). For further structural correlation analysis, the characterization of SAXS and SANS is considered. The respective log-log intensity is reported in Figure 8.2 (a). The fitting of the SAXS intensity profile provides the idea of constituent primary MNPs structural behaviour. However, three various contributions are used for fitting various form factor parameters. The fitting parameter contribution 1 is similar to Chapter 3, in which the homogenousXS model is used as a form factor having a delta distribution function (28).

The observed parameters after fitting confirm the existence of nanoflakes as primary MNP shapes having 5 nm thickness and 36 nm diameter. Additionally, the spherical model form factor with log-normal distribution is considered. The presence of isotropic nanoparticles is confirmed with 8.5 nm of radius having polydispersity of 0.38 and there is no structure factor contribution. This contribution arises from Nickel Ferrite isotropic MNPs. In addition, in another contribution, the spherical form factor is seen as having a 3.5 nm radius
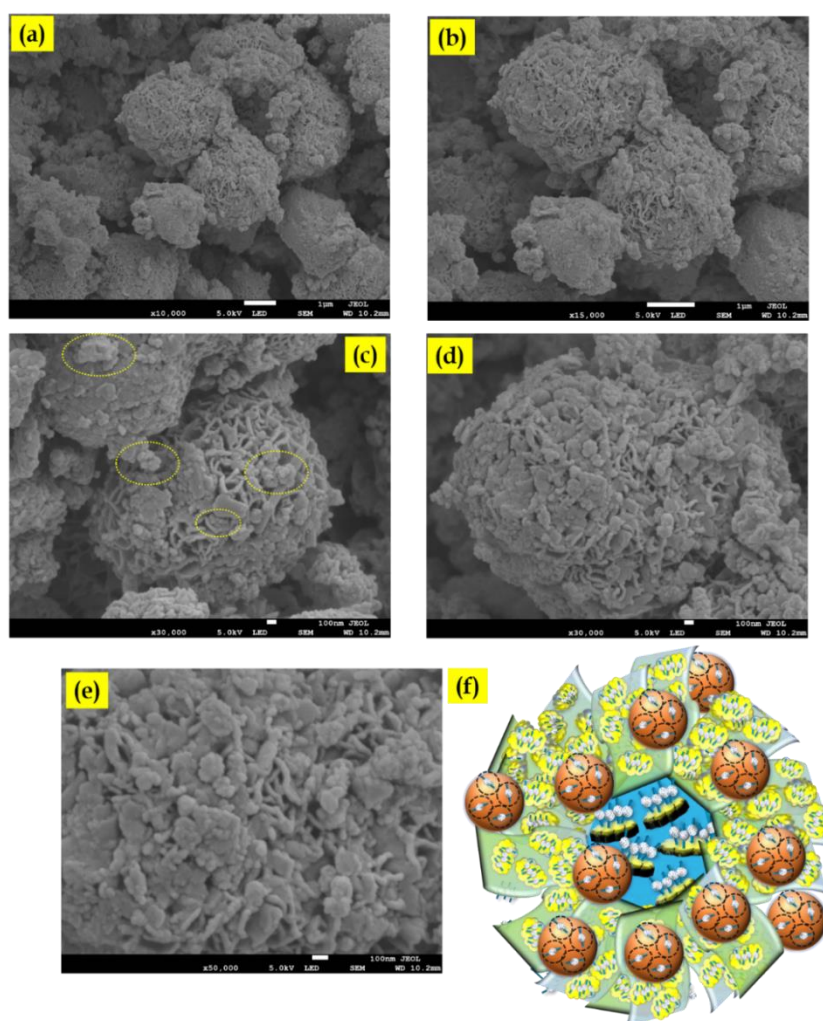
Figure 8.1: FESEM images at a resolution (a) 1 µm scale bar, (b) 100 nm scale bar, (c) 1 µm scale bar, (d) 100 nm scale bar, and (e) 100 nm scale bar, and (f) Schematic representation of hybrid ensemble of γ-Fe$_2$O$_3$@δ-MnO$_2$@NiFe$_2$O$_4$. The schematic is depicted wherein three different nanosystems are presented to differentiate among Nickel Ferrite nanoparticles (presented in the core), δ-MnO$_2$ nanoflakes, and Iron Oxide nanoparticles over the flakes. Iron Oxide is decorated over the system MnO$_2$@NiFe$_2$O$_4$ (which is used in Chapter 3 for magnetic analysis wherein TEM images of MnO$_2$@NiFe$_2$O$_4$ are shown). The decoration of Iron Oxide over the ensemble of MnO$_2$@NiFe$_2$O$_4$ in yellow circle in Figure (c). The spin arrangement is also shown in the Schematic to illustrate the alignment of the blocked spins.

with a polydispersity index of magnitude 0.35. In this contribution, the mass fractal structure factor is observed. A value of size aggregation of 100 with a fractal dimension of 1.7 is achieved. In the higher q range, an additional contribution is added following log-normal distribution of 1 nm radius and polydispersity of 0.5. Such contribution is because of interparticle spacing among MNPs. In the lower q range, the SANS intensity profile gives information about secondary ensembles. The existence of two varied-sized ensembles is expected from the SANS profile [28]. The fitting provides a diameter having 466 nm for the ensemble with a polydispersity index of 0.05. As seen in the FESEM micrograph, maghemite MNPs are observed to form an additional assembly, which is ensured by the one more fitting contribution achieved from SANS profile fitting having 41.5 nm radius and 0.280 polydispersity index.

For crystal phase confirmation, XRD analysis is performed [26, 27]. The maghemite (γ-Fe_2O_3) phase development is confirmed from the respective planes (111), (211), (220), (311), (222), (400), (422), (511), (440), and (620) having JCPDS number of 39-1346, Nickel Ferrite ($NiFe_2O_4$) phase formation is confirmed from the planes (220), (311), (400), (422), (511), (440), and (533) with JCPDS number of 10-0325, and the respective δ-MnO_2 phase is ensured from (001), (002), ($\bar{1}$11), and (020) planes having JCDPS no. of 80-1098, as depicted in Figure 8.2 (b). The Raman spectra is executed in order to confirm the crystalline phase [26, 27, 30, 31, 32, 33] as depicted in Figure 8.2 (c). The peaks at 497, 660, and 730 cm^{-1} are due to γ-Fe_2O_3 phase which is obtained after deconvolution. An additional characteristic peak is achieved at 1325 cm^{-1} for the maghemite phase. The obtained peaks are vibration modes of O_h^7(Fd3m) for γ-Fe_2O_3. The obtained band at 640 cm^{-1} is in A_{1g} symmetric mode for stretching vibration, ν_2(Mn–O). The other band at 568 cm^{-1} is symmetric ν_3(Mn-O) stretching vibration mode. The 660 cm^{-1} band is A_g symmetry mode related to the tetrahedral AO_4 group of Nickel Ferrite. The respective bands of F_{2g} at 568 cm^{-1} and 470 cm^{-1} are due to the octahedral stretching mode of nickel ferrite [32].
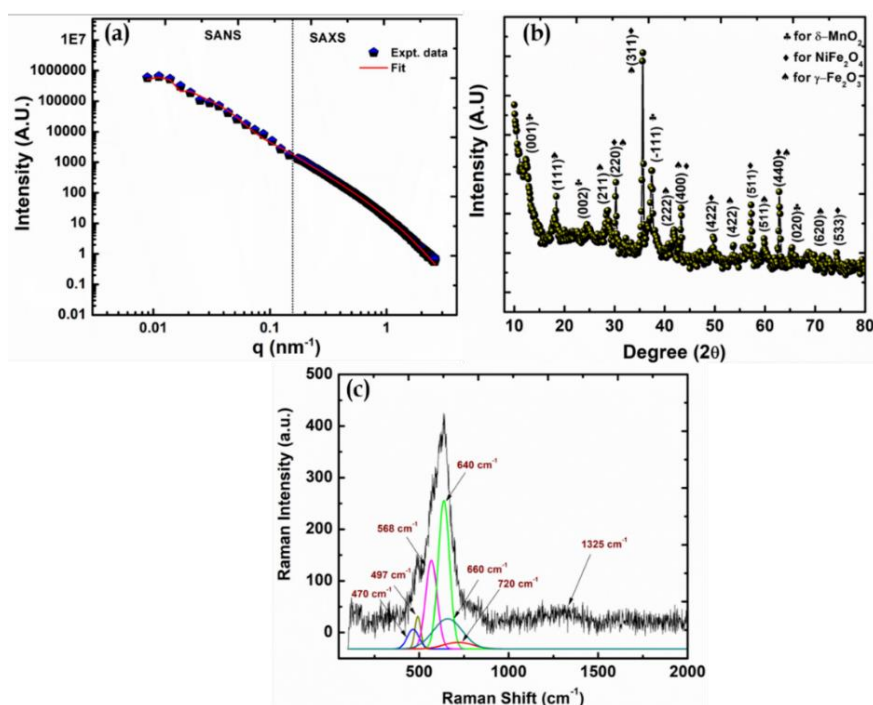
Figure 8.2: (a) SAXS and MSANS intensity profile, (b) XRD curve, and (c) Raman spectrum of γ-Fe$_2$O$_3$@δ-MnO$_2$@NiFe$_2$O$_4$.

The XPS pattern is represented in Figure 8.3, for chemical composition information, in which binding energy distribution is addressed. The Mn 2p peak is found to be consisted of peaks at 642.1 eV for $2P_{3/2}$ and 653.9 eV for $2P_{1/2}$ as seen in Figure 8.3 (a) [30]. The four respective peaks of Nickel 2P are shown in Figure 8.3(b) to confirm that $2P_{3/2}$ and $2P_{1/2}$ have binding energy of 855 eV and 872.3 eV, and two satellite peaks are found at 860 eV and 875.6 eV [34]. The satellite peaks are due to the +2 oxidation state of nickel ferrite. The Fe 2P splitting are shown at 710.8 eV for Fe $2P_{3/2}$ and 724.3 eV for Fe $2P_{1/2}$ [34] as given in Figure 8.3(c). The higher area is covered by Fe $2P_{3/2}$ than Fe $2P_{1/2}$ which confirms j-j coupling, having 4 degeneracy of Fe $2P_{3/2}$ in contrast to 2 degeneracy of Fe $2P_{1/2}$. The satellite peaks are seen at 714.1 eV and 718.4 eV respectively, related to Fe^{3+} ions [34, 35]. A broad O 1s spectrum is achieved at 7 eV width [30, 34, 35] as depicted in Figure 8.3(d) and from deconvolution, peaks are found at 533.5 eV, 531.3 eV, and 529.7 eV. A characteristic peak at 529.7 eV is due to the surface lattice of O^{2-} ions, which is found in γ-Fe$_2$O$_3$/MnO$_2$/NiFe$_2$O$_4$. The general

oxygen defects are seen in the metal oxide framework, which provides enhanced binding energy at 531.3 eV because of oxygen vacancies. The observed peak at 533.5 eV is due to the existence of a hydroxyl group (Metal-OH).
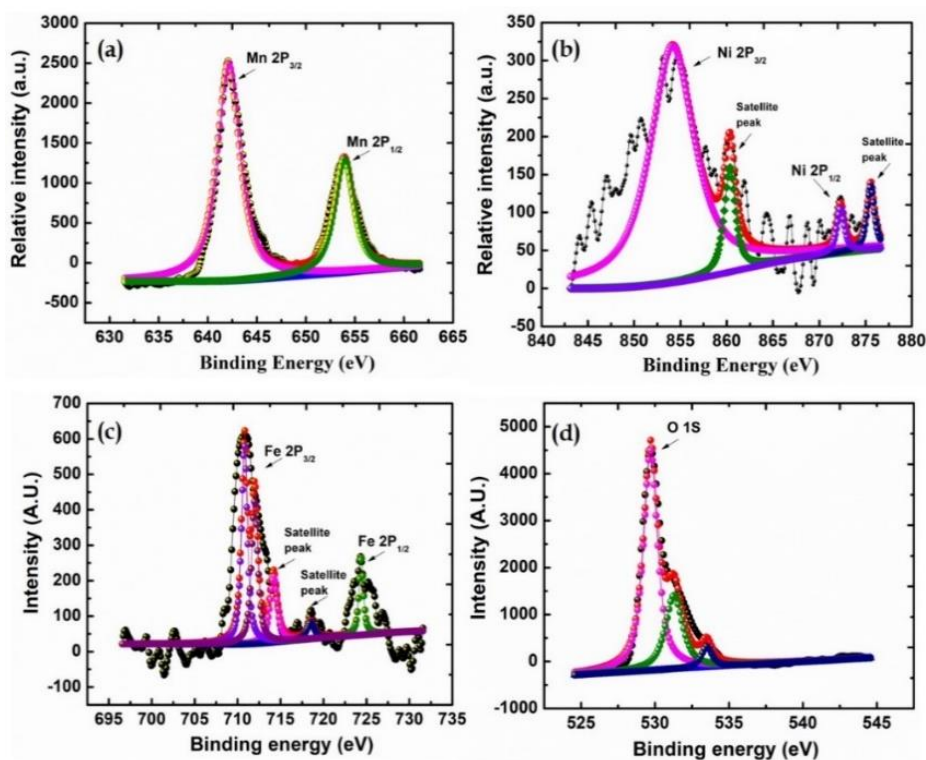

Figure 8.3: XPS analysis for (a) Mn 2P, (b) Ni 2P, (c) Fe 2P, and (d) O 1S spectrum of γ-Fe$_2$O$_3$@δ-MnO$_2$@NiFe$_2$O$_4$.

Further, elementary composition is confirmed by the EDS study as given in Figure 8.4. The existence of Manganese (Mn), Iron (Fe), Nickel (Ni), and Oxygen (O) is ensured with the aid of elementary mapping having atomic percentages varied from 30.32 %, 22.41%, 1.96%, and 54.05% for the mentioned metals. Therefore, the development of γ-Fe$_2$O$_3$@δ-MnO$_2$@NiFe$_2$O$_4$ is ensured from the entire microstructural analysis. Such a system with an interesting hierarchy arrangement can be considered for understanding spin dynamics by considering ac susceptibility study.
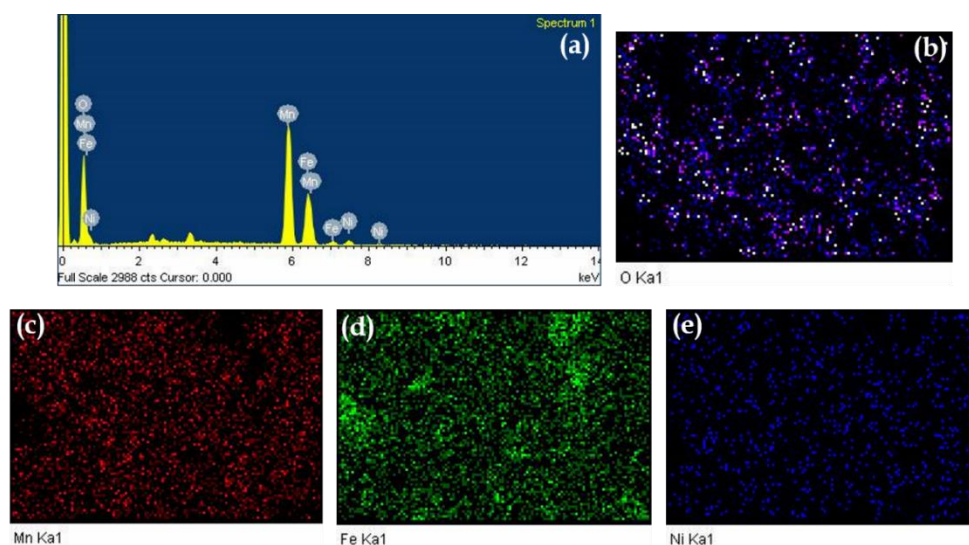
Figure 8.4: (a) Sum spectrum of EDX, (b) elementary mapping for O, (c) elementary mapping for Mn, (d) elementary mapping for Fe, and (e) elementary mapping for Ni of γ-Fe_2O_3@δ-MnO_2@$NiFe_2O_4$.

Table 8.1 Elementary composition achieved from EDX analysis.

Element	Weight %	Atomic %
Mn	48.85	30.32
Ni	3.38	1.96
Fe	22.41	13.68
O	25.36	54.05

8.3.2 Dynamic Magnetic study

The phase transition in spin dynamics of the hybrid ensemble is studied considering frequency dependence ac susceptibility [36]. A temperature range of 5-350 K is considered without any DC field and with a 10 Oe exciting ac field. The in-phase and out-of-phase ac susceptibility is given in Figure 8.5. A variation with applied frequency variance is seen with a range of frequencies as, 93 Hz, 317

Hz, 717 Hz, 1111 Hz, 3717 Hz, 6717 Hz, and 9724 Hz, and frequency-dependent peak is observed to get shifted toward high-temperature domain with an increase in frequency. The peak shift with frequency is due to enhancement in the delay of spin-relaxation [36]. The calculated Mydosh parameter value is achieved as 0.05, further confirming the possibility of finite interaction in MNPs. The presence of a non-zero imaginary of ac susceptibility trend as depicted in Figure 8.5 (b) is due to moment-induced absorption along with displacement in the irreversible domain wall. In the imaginary component, two peaks are seen at 110 K and 41 K, at high-frequency condition. The presence of such additional peak is
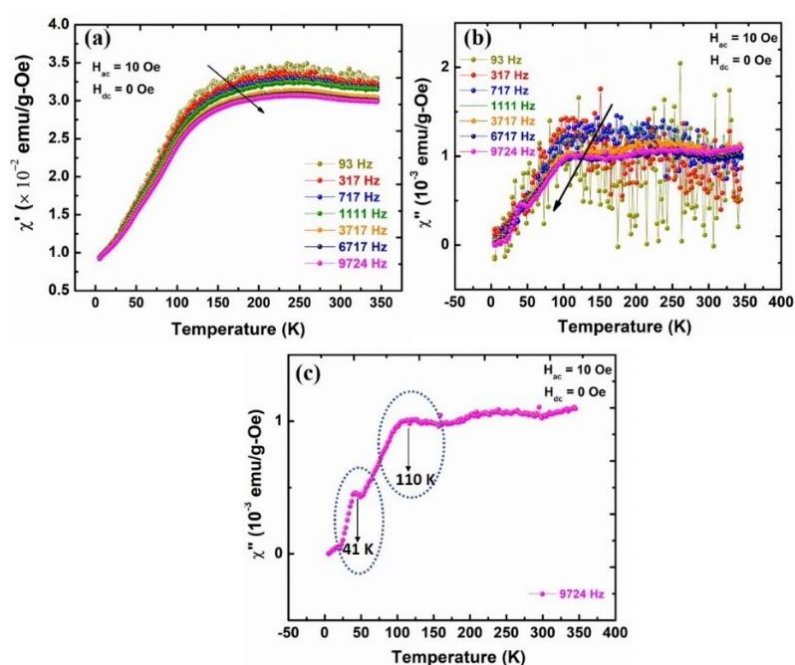

Figure 8.5: (a) In-phase ac susceptibility with different frequencies, (b) out-of-phase ac susceptibility with frequencies for γ-Fe$_2$O$_3$@δ-MnO$_2$@NiFe$_2$O$_4$, (c) depiction of two peaks in out-of-phase component at frequency of 9724 Hz (two different T_{max} are shown in circle). The arrow mark indicates the change in T_{max} and χ_{max} with an increase in frequency in Figure (a, b).

generally observed because of core-shell morphology [48]. The peak at high temperature is because of SPM blocking and the peak at low temperature is

because of low temperature spin freezing. However, the organization of MNPs can trigger such dual peak in imaginary component.
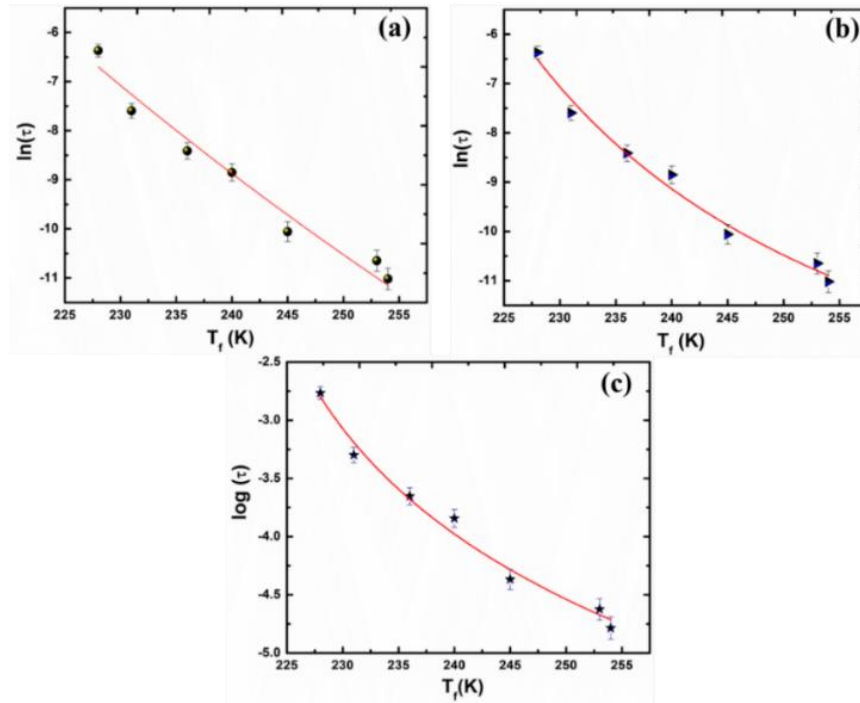

Figure 8.6: Temperature maxima fitting with a range of frequency following: (a) Neel-Brown model, (b) VF model, and (c) Critical slowing down model of γ-$Fe_2O_3@\delta$-$MnO_2@NiFe_2O_4$. The error bars in the data represent standard deviation in experimental data.

In the case of non-interacting MNPs, the spin blocking with varied frequency can be explained by the Neel-Arrhenius equation, which is given in equation 2.10 of Chapter 2. For SPM systems, the respective spin relaxation period, τ_0, lies in the 10^{-9} to 10^{-13} s order range. Generally, blocking temperature gives the idea about the needed potential energy to overcome energy barriers [52]. The frequency-dependent temperature anomaly as observed in in phase ac susceptibility is fitted with Neel-Arrhenius law, as depicted in Figure 8.6(a), which gives unphysical τ_0 of ~ 1.6×10^{-22} s and respective activation energy, $\frac{E_a}{k_B}$ ~ 9910.6 K. The observed unphysical value discards the possibility of a non-interacting SPM state [36, 37]. Therefore, the possible interaction among MNPs of the ensemble is anticipated.

The existence of interaction can influence the blocking temperature, which results in potential barrier modulation.

In addition, the shifting in temperature maxima with frequency is further examined by Vogel-Fulcher (VF) law, as given in equation 2.11 of chapter 2, [depicted in Figure 8.6(b)]. The fitted values give flipping period, τ_0 , VF temperature, T_0 and activation energy, $\frac{E_a}{k_B}$ as τ_0 = 0.5 × 10^{-9} s, T_0 = 192.9 K, and $\frac{E_a}{k_B}$ = 361 K respectively. The values show a good agreement with VF-model, confirming the existence of finite interaction among MNPs of the ensemble [39, 36]. The energy barrier is achieved as 4.98× 10^{-14} erg, further confirming the existence of enhanced anisotropy. For more detailed evaluation, the Tholence criterion [40] is calculated as, δT_{Th} = $\frac{T_f - T_0}{T_f}$ and yields a value of 0.15. The reduction of δT_{Th} from unity confirms the presence of finite interaction in the ensemble [36, 37].

Moreover, for a detailed investigation of whether the spin dynamics is dominated by spin blocking or spin freezing, a critical slowing model is considered, as mentioned in equation 2.13 of chapter 2. After non-linear curve fitting as depicted in Figure 8.6(c), the best fitting is achieved as relaxation period, τ^* = 3.9 × 10^{-8} s, critical exponent, zv' = 3.4, and glass transition temperature, T_g = 217 K, respectively. For conventional SG system, zv' comes in 4 -12 range with τ^* of 10^{-10} -10^{-12} order. In addition, a few cluster SG systems show 10^{-8} s order for τ^* [25]. In the current scenario, τ^* is slightly varying from the relaxation period achieved from VF-fitting, but zv' confirms the non-existence of conventional SG behaviour. Therefore, all the findings ensure the existence of moment blocking in the system [39].

8.3.3 MR-relaxivity:

Before performing MR-relaxivity analysis, Zeta potential analysis and biological compatibility is performed. The respective plot of the Zeta potential plot is
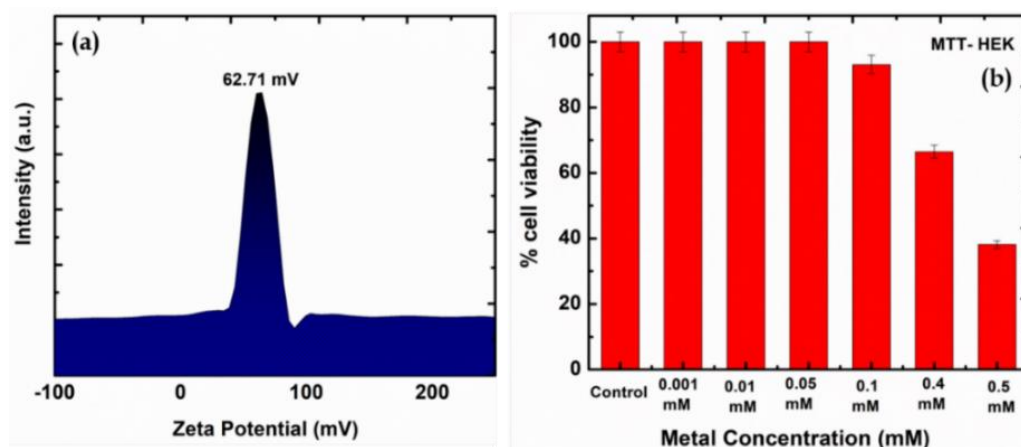
Figure 8.7: (a) Zeta potential curve, (b) MTT-based cytotoxicity analysis study for HEK-293 cell-line of γ-Fe$_2$O$_3$@δ-MnO$_2$@NiFe$_2$O$_4$. The error bars are for standard deviation representation
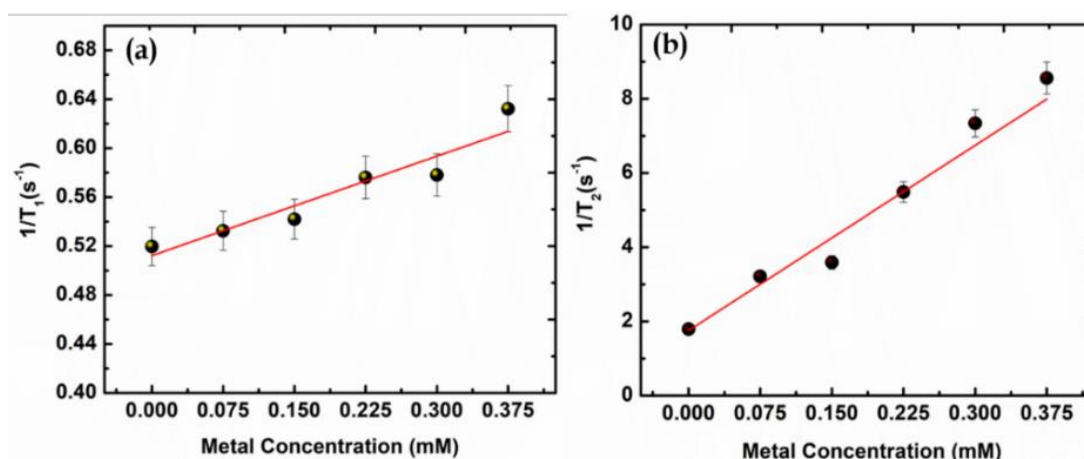
Figure 8.8: MR-relaxation analysis of γ-Fe$_2$O$_3$@δ-MnO$_2$@NiFe$_2$O$_4$: (a) Longitudinal relaxivity (r$_1$) and (b) transverse relaxivity (r$_2$) plot with various concentrations. The error bars are for standard deviation representation.

depicted in Figure 8.7 (a). The steric stabilization is confirmed by Zeta potential value of 62.7 mV [19]. However, cell viability in an agarose stabilized system is performed with HEK-293 cell lines following MTT assay [19]. The metal concentrations are considered as, 0.001, 0.01, 0.05, 0.1, 0.4, and 0.5 mM. In Figure 8.7 (b), the cell viability with various MNPs concentration is shown for an incubation period of 24 h. An acceptable cell viability is observed till a metal

concentration of 0.4 mM. However, at 0.5 mM, cell viability is found to reduce below 40%. Therefore, for the MR-relaxivity study, the considered meal concentration is below the 0.4 mM limit.
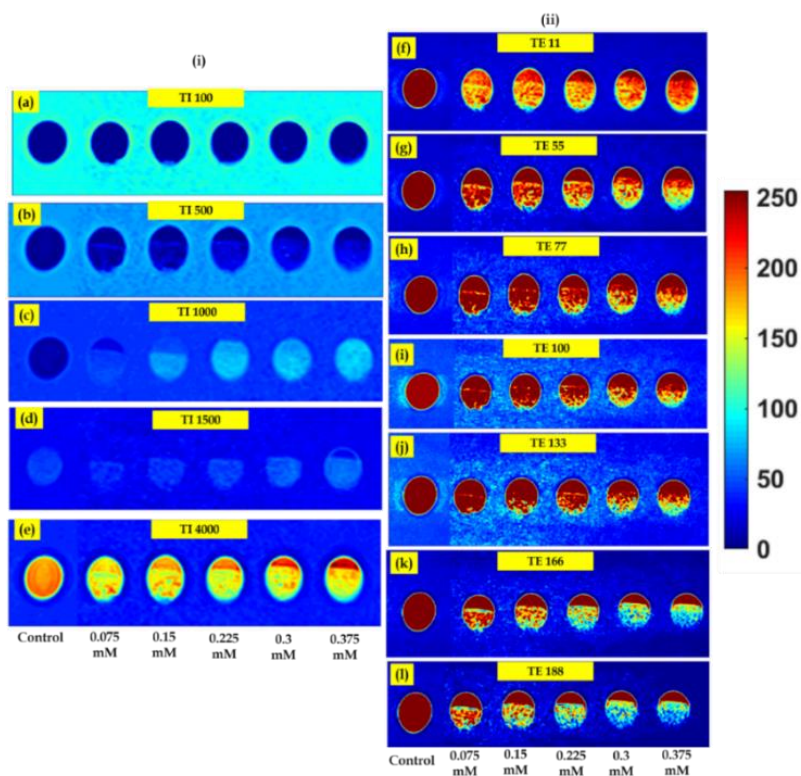

Figure 8.9: Phantom image of γ-Fe$_2$O$_3$@δ-MnO$_2$@NiFe$_2$O$_4$: (i) Longitudinal relaxation at different inversion time (TI) (a-e) and (ii) Transverse relaxation at different echo time (TE) (f-l) with metal concentrations variation.

To execute MR-relaxivity analysis, a series of metal concentrations are considered as, 0.0750, 0.150, 0.150, 0.225, 0.300, and 0.375 mM respectively. The MNPs are stabilized in a solution of agarose. The considered control is the stabilized agarose. To calculate longitudinal relaxivity, the signal intensity (M_{TI}) is fitted following equation 5.8 of Chapter 5 for all metal concentration considering variation in inversion time (TI). TI is varied from 100 to 4000 ms with 5000 ms TR and 12 ms TE. The calculated longitudinal relaxivity time, marked as T$_1$, for all metal concentrations is addressed. To achieve longitudinal relaxation rate r$_1$, a plot is addressed with
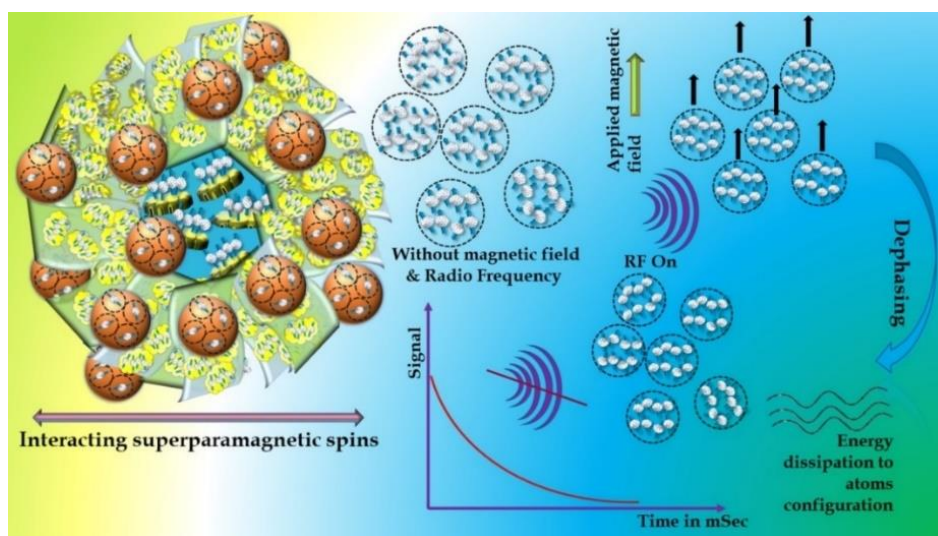
Figure 8.10: Schematic of spin organization in interacting superparamagnetic ensembles having both isotropic and anisotropic MNPs with significant MR-relaxivity of γ-Fe$_2$O$_3$@δ-MnO$_2$@NiFe$_2$O$_4$.

respective $1/T_1$ for each considered metal concentration as depicted in Figure 8.8(a), following equation 5.9 of Chapter 5. For, transverse relaxivity, the respective signal intensity (M_{TE}) having various echo times (TE) is fitted with equation 5.10 of Chapter 5. A non-linear curve fitting is employed and a transverse relaxivity period, T_2, for each metal concentrations is achieved, which is further considered for fitting as, $1/T_2$ versus respective metal concentration. The obtained slope gives a transverse relaxation rate, r_2 as displayed in Figure 8.8(b). r_2 and r_1 values are achieved as 16.67 mM^{-1}s^{-1} and 0.27 mM^{-1}s^{-1} at 3 T, with r_2/r_1 of 61.5. The obtained r_2/r_1 ensures potential contrast behaviour [19, 40, 41]. As the obtained r_2/r_1 is higher than that of 10, the transverse relaxivity dominance is present in the system. Hence this system is a good candidate for T_2 type contrast in MRI. Further, phantom images are depicted in Figure 8.9 with variation of TI and TE at all the metal concentrations. As given in Figure 8.9(i), T_1-based *in vitro* MR-phantom images shows an enhancement of signal brightness with an increment in metal concentration. The inversion time is varied as, 100, 500, 1000, 1500, and 4000 ms as given in Figure 8.9(i (a-e)). The respective signal brightness enhancement is reflected with inversion time enhancement, as

depicted in Figure 8.9(i (a-e)). However, the dark contrast of T_2 *in vitro* MR-phantom images is enhanced with increase in metal concentration as depicted in Figure 8.9(ii). The variation in echo period is considered as, 11 ms, 55 ms, 77 ms, 100 ms, 133 ms, 166 ms, and 188 ms respectively. The increment in signal intensity is reflected with enhanced echo time as depicted in Figure 8.9(ii(f-l)). Such enhancement shows significant capability of considered hybrid ensemble for achieving efficient T_2-based contrast imaging in the MRI.

8.4 CONCLUDING REMARKS

Herein conclusion, the hybrid ensemble is considered for MR- transverse relaxivity enhancement with signal regulation, considering significant r_2/r_1 values. The hierarchical ensemble, γ-Fe_2O_3@δ-MnO_2@$NiFe_2O_4$, shows a cell viable nature with structural correlation property. The spin dynamic nature is addressed from ac susceptibility study having 4.98×10^{-14} erg energy barrier with a spin flipping period of 0.5×10^{-9} s. However, the respective Mydosh parameter as well as the Tholence criterion confirms the dominance of the interacting SPM state, which is further confirmed by critical slowing down fitting and non-zero VF temperature. The proton diffusion is found to be faster around the considered interacting SPM hybrid ensemble with enhanced r_2/r_1 of 61.5. The interacting SPM domains of hierarchical ensemble having regulated activation energy is a potential approach to achieve enhanced MR-transverse relaxivity.

References:

[1] MacMahon, E. and Brougham, D. F. pH Dependence of MRI Contrast in Magnetic Nanoparticle Suspensions Demonstrates Inner-Sphere Relaxivity Contributions and Reveals the Mechanism of Dissolution. *Langmuir*, 39:2171-2181, 2023.

[2] Hayashi, K., Sato, Y., Sakamoto, W. and Yogo, T. Theranostic Nanoparticles for MRI-Guided Thermochemotherapy: "Tight" Clustering of Magnetic

Nanoparticles Boosts Relaxivity and Heat-Generation Power. *ACS Biomaterials Science & Engineering,* 2017, 3, 1, 95–105.

[3] Miao, Y., Zhang, H., Cai, J., Chen, Y., Ma, H., Zhang, S., Bao, J., Liu, X., Bay, B., Guo, Y., Gu, N. and Fan, H. Structure–Relaxivity Mechanism of an Ultrasmall Ferrite Nanoparticle T_1 MR Contrast Agent: The Impact of Dopants Controlled Crystalline Core and Surface Disordered Shell. *Nano Letters,* 21:1115, 2021.

[4] Culver, K., Shin, Y. J., Rotz, M. W., Meade, T. J., Hersam, M. C. and Odom, T. W. Shape-Dependent Relaxivity of Nanoparticle-Based T1 Magnetic Resonance Imaging Contrast Agents, The Journal of Physical Chemistry C, 120:22103, 2016.

[5] Antal, I., Strbak, O., Khmara, I., Koneracka, M., Kubovcikova, M., Zavisova, V., Kmetova, M., Baranovicova, E. and Dobrota, D. MRI Relaxivity Changes of the Magnetic Nanoparticles Induced by Different Amino Acid Coatings. *Nanomaterials*, 10: 394, 2020.

[6] Brooks, R.A., Moiny, F., Gillis, P. On T_2-Shortening by Weakly Magnetized Particles: The Chemical Exchange Model. *Magnetic Resonance in Medicine*, 1020: 1014, 2001.

[7] Jensen, J.H. and Chandra, R. NMR relaxation in tissues with weak magnetic inhomogeneities. *Magnetic Resonance in Medicine*. 44;144, 2000.

[8] Yablonskiy, D.A. and Haacke, E.M. Theory of NMR Signal Behavior in Magnetically Inhomogeneous Tissues: The Static Dephasing Regime. *Magnetic Resonance in Medicine*, 32:749, 1994.

[9] Brooks, R.A. T_2-shortening by strongly magnetized spheres: A chemical exchange model. *Magnetic Resonance in Medicine*, 47:388, 2002.

[10] Gillis, P., Moiny, F. and Brooks, R. A. On T2-shortening by strongly magnetized spheres: A partial refocusing model. *Magnetic Resonance in Medicine*, 47:257, 2002.

[11] Chen, D.X.; Sun, N.; Huang, Z.J.; Cheng, C.M.; Xu, H.; Gu, H.C. Experimental study on T2 relaxation time of protons in water suspensions of iron-oxide nanoparticles: Effects of polymer coating thickness and over-low $1/T_2$. *Journal of Magnetism and Magnetic Materials*. 322:548, 2020.

[12] Matsumoto, Y. and Jasanoff, A. T_2 relaxation induced by clusters of superparamagnetic nanoparticles: Monte Carlo simulations. *Magnetic Resonance Imaging*, 26:994, 2008.

[13] Boxerman, J.L., Hamberg, L.M.; Rosen, B.R. and Weisskoff, R.M. Mr contrast due to intravascular magnetic susceptibility perturbations. *Magnetic Resonance in Medicine*, 34:555, 1995.

[14] Laurent, S., Forge, D., Port, M., Roch, A., Robic, C., Vander Elst, L., Muller, R.N. Magnetic iron oxide nanoparticles: Synthesis, stabilization, vectorization, physicochemical characterizations, and biological applications. *Chemical Reviews*, 108:2064, 2008.

[15] Villaraza, A.J.L., Bumb, A., and Brechbiel, M.W. Macromolecules, dendrimers, and nanomaterials in magnetic resonance imaging: The interplay between size, function, and pharmacokinetics. *Chemical Reviews*, 110:2921, 2010.

[16] Yang, L., Wang, Z., Ma, L., Li, A., Xin, J., Wei, R., Lin, H., Wang, R., Chen, Z., and Gao, J. The Roles of Morphology on the Relaxation Rates of Magnetic Nanoparticles. *ACS Nano*, 12:4605, 2018.

[17] Zhou, Z., Zhao, Z., Zhang, H., Wang, Z., Chen, X., Wang, R., Chen, Z., and Gao, J. Interplay between Longitudinal and Transverse Contrasts in Fe3O4 Nanoplates with (111) Exposed Surfaces. *ACS Nano*, 8, 7976:2014.

[18] Zhou, Z., Tian, R., Wang, Z., Yang, Z., Liu, Y., Liu, G., Wang, R., Gao, J., Song, J., Nie, L., and Chen, X. Artificial local magnetic field inhomogeneity enhances T2 relaxivity. *Nature Communications*, 8:15468, 2017.

[19] Konwar, K., Sharma, N., Pranjali, P., Guleria, A., Kaushik, S.D., Dutta, A., Mukhopadhyay, R., Sen, D., Gao, W. and Deb, P., Structure-Correlated Magnetic Resonance Transverse Relaxivity Enhancement in Superparamagnetic Ensembles with Complex Anisotropy Landscape. *Langmuir*, 38:11087, 2022.

[20] Zhou, Z., Bai, R., Munasinghe, J., Shen, Z., Nie, L. and Chen, X. T_1–T_2 Dual-Modal Magnetic Resonance Imaging: From Molecular Basis to Contrast Agents. *ACS Nano*, 11:5227, 2017.

[21] Simsek, T. and Özcan, S. Effective magnetic anisotropy enhancement of FePt nanocrystals through shape control. *Journal of Magnetism and Magnetic Materials*, 351:47, 2014.

[22] Nina Kostevsek, A Review on the Optimal Design of Magnetic Nanoparticle-Based T_2 MRI Contrast Agents, *Magnetochemistry*, 6:11, 2020.

[23] Reyes-Ortega, F., Delgado, A. V. and Iglesias, G. R. Modulation of the Magnetic Hyperthermia Response Using Different Superparamagnetic Iron Oxide Nanoparticle Morphologies, *Nanomaterials*, 11:627, 2021.

[24] Aflori, M. Smart Nanomaterials for Biomedical Applications—A Review, *Nanomaterials*, 11:396, 2021.

[25] Zhou, Z., Yang, L., Gao,J. and Chen, X. Structure–Relaxivity Relationships of Magnetic Nanoparticles for Magnetic Resonance Imaging, *Advanced Materials*, 31:1804567, 2019.

[26] Xiang, B., Ling, D., Lou, H. and Gu, H. 3D hierarchical flower-like nickel fe6rrite/manganese dioxide toward lead (II) removal from aqueous water, *Journal of Hazardous Materials*, 325:178, 2016.

[27] Saikia, K., Sarma, D. D. and Deb, P. Organization dependent collective magnetic properties of secondary nanostructures with differential spatial

ordering and magnetic easy axis orientation. *Journal of Magnetism and Magnetic Materials*,127:2016408, 2016.

[28] Kohlbrecher, J. SASfit: A program for fitting simple structural models to small angle scattering data, 2023.

[29] Saikia, K., Kaushik, S.D., Sen, D., Mazumder, S. and Deb. P. Fatty acid as structure directing agent for controlled secondary growth of $CoFe_2O_4$ nanoparticles to achieve mesoscale assemblies: A facile approach for developing hierarchical structures, *Applied Surface Science*, 379:530, 2016.

[30] Cremonezzi, J. M. O., Tiba, D. Y. and Domingues, S. H. Fast synthesis of δ-MnO_2 for a high-performance supercapacitor electrode, *SN Applied Sciences,* 2:1689, 2020.

[31] Testa-Anta, M., Ramos-Docampo, M.A., Comesa̅na-Hermo, M, Rivas-Murias, Beatriz and Salgueiri̅no, V. Raman spectroscopy to unravel the magnetic properties of iron oxide nanocrystals for bio-related applications, *Nanoscale Advances,* 1:2086, 2019.

[32] Soam, A. Kumar, R., Thatoi, D. and Singh, M. Electrochemical Performance and Working Voltage Optimization of Nickel Ferrite/Graphene Composite based Supercapacitor, *Journal of Inorganic and Organometallic Polymers and Materials*, 30:3325, 2020.

[33] Hanesch, M. Raman spectroscopy of iron oxides and (oxy)hydroxides at low laser power and possible applications in environmental magnetic studies, *Geophysical Journal International,* 177:941, 2009.

[34] Hua, M., Xu, L., Cui, F., Lian, J., Huang, Y., Bao, J., Qiu, J., Xu, J., Xu, H., Zhao,Y. and Li, H. Hexamethylenetetramine-assisted hydrothermal synthesis of octahedral nickel ferrite oxide nanocrystallines with excellent supercapacitive performance, *Journal of Material Sciences,* 53:7621, 2018.

[35] Jain, S., Shah, J., Negi, N. S., Sharma, C. and Kotnala, R. K. Significance of interface barrier at electrode of hematite hydroelectric cell for generating ecopower by water splitting, *International Journal of Energy Research*, 43:4743, 2019.

[36] Konwar, K., Kaushik, S.D., Sen, D. and Deb, P; Dynamic spin freezing and magnetic memory effect in ensembles of interacting anisotropic magnetic nanoparticles. *Physical Review B*. 102:174449, 2020.

[37] Bag, P., Baral, P. R. and Nath, R. Cluster spin-glass behavior and memory effect in Cr0.5Fe0.5Ga, Physical Review B, 98: 144436, 2018.

[38] Stimpson, L. J. V., Powell, J. M., Stenning, G. B. G., Jura, M. and Arnold, D. C. Spin-glass behavior in KxRu4−yNiyO8 hollandite materials, Phy. Rev. B. 98:174429, 2018.

[39] Usov, N. A. and Serebryakova, O. N. Equilibrium properties of assembly of interacting superparamagnetic nanoparticles, *Scientific Reports*, 10:13677, 2020.

[40] Guleria, A., Pranjali, P., Meher, M. K., Chaturvedi, A., Chakraborti, S., Raj, R., Poluri, K. and Kumar, D. Effect of Polyol Chain Length on Proton Relaxivity of Gadolinium Oxide Nanoparticles for Enhanced Magnetic Resonance Imaging Contrast. *J. Phys. Chem. C*, 123:18061, 2019.

[41] Thapa, B., Diaz-Diestra, D., Badillo-Diaz, D., Sharma, R., Dasari, K., Kumari, S., Holcomb, M., Beltran-Huarac, J., Weiner, B. and Morell, G. Controlling the transverse proton relaxivity of magnetic graphene oxide. *Scientific Reports*, 9:5633, 2019.